Second International Symposium on Marine Propulsors
smp'11, Hamburg, Germany, June 2011

Hydroelastic Response and Stability of a Hydrofoil in Viscous Flow

Antoine Ducoin, Yin Lu Young

University of Michigan, Department of NAME, Ann Arbor, Michigan, USA

ABSTRACT

The objective of this research is to investigate the hydroelastic response and stability of a flexible hydrofoil in viscous flow. The effects of fluid viscosity, such as laminar to turbulent transition and stall, on the fluid-structure interaction (FSI) response and divergence speed prediction are presented. The numerical approach is based on the coupling between a commercial Computational Fluid Dynamics (CFD) solver, CFX, and a simple two-degrees-of-freedom (2-DOF) system that simulates the free tip section displacement of a cantelivered, rectangular hydrofoil. The method is validated by comparing numerical predictions with experimental measurements of a rigid (stainless steel) and a flexible (POM Polyacetate) hydrofoil. The Reynolds number varied from 0.75×10^6 to 3×10^6, and the initial angle of attack varied from 2° to 8°. The effects of transition and stall on the hydrodynamic coefficients, pressure distribution, center of pressure, foil deformations, and static divergence velocity are presented. At low to moderate initial static angles of attack (α_0), nonlinear effect due to transition significantly decreases the slope of the lift curve, which leads to an increase of the divergence velocity. At high angles of attack, the effective angle of attack ($\alpha_{eff}= \alpha_0+ \theta_0$, where θ_0 is the tip twist angle) increases nonlinearly with increasing load because of the increase in moment created by the shifting of the center of pressure toward the foil leading edge. The slope of effective lift curve decreases with the development of flow separation until it becomes negative when stall occurs, which helps to delay static divergence.

Keywords

Hydroelasticity, fluid-structure interaction, hydrofoil, viscous effects, static divergence, incompressible flow

1 INTRODUCTION

Flexible lifting bodies, such as high aspect ratio, highly skewed, or self-adaptive blades, wings, and hydrofoils, may be subject to hydroelastic instabilities such as static divergence, flutter, resonance, etc. Static divergence of a flexible hydrofoil occurs when the deflection induced by the hydrodynamic load results in a further increase in deflection until the structure's twisting capacity is reached or material failure develops. Static divergence of flexible lifting bodies has been the subject of much research in aeroelasticity because of high aspect ratio, lightweight, flexible aircraft blades, wings, and airfoils. Excellent introductions to aeroelasticity, including static divergence and flutter, could be found in classic texts such as Fung (1955) and Bisplinghoff et al (1955). The effects of material properties and geometry on the subcritical, static, aeroelastic wing response and on the divergence speed were studied in Librescu & Thangjitham (1991). More recently, Librescu & Maalawi (2009) presented an optimization method, which maximizes the divergence speed without having to increase the structural mass. In Thomas et al (2002), nonlinear aerodynamic effects on divergence, flutter, and limit cycle oscillation of a transonic airfoil wing were studied using a single-degree-of-freedom model. The influence of the center of pressure location on large amplitude pitch motion was highlighted. Finally, in Edwards & Wieseman (2008), the generalized aeroelastic analysis method was applied to illustrate divergence and flutter instabilities on an airfoil. A finite element code and a generalized doublet lattice method were used. It was shown that the divergence and flutter velocities highly depend on the center of gravity of the airfoil, and good agreement was found between the numerical predictions and experimental measurements.

Although static divergence has received much attention in the past five decades, analytical and numerical investigations thus far focused on inviscid fluids for aerospace or wind turbine applications. Nevertheless, static divergence can also occur on marine blades and hydrofoils, such as when a highly skewed and/or flexible composite propeller operates in a crashback mode. In such scenarios, viscous effects are not negligible due to the reduction in relative in flow velocity, high fluid viscosity, and high angles of attack and flow separation caused by the reversed flow, see Chang et al (2008). Hence, the objective of this paper is to investigate the hydroelastic response and stability of a flexible hydrofoil in viscous flow, with focus on the effects of FSI response on laminar to turbulent transition, stall, and static divergence. The goal is to gain insights into the governing physics to avoid static divergence failure of self-adaptive composite propellers, hydrofoils, rudders, etc.

At moderates Reynolds numbers, the boundary layer flow can be transitional around the lifting body. A separated flow region due to adverse pressure gradient typically triggers the transition. The development of turbulent flow, which causes a momentum transfer normal to the wall, allows the flow to re-attach, and form a so-called Laminar Separation Bubble (LSB) (Gaster 1969). It has been shown that the LSB first appears near the trailing edge for low to moderate angles of incidence, and then moves towards the leading edge as the angle of incidence increases (Ducoin et al 2009a). The movement of the LSB affects the hydrodynamic and vibration characteristics, as shown in Poirel et al (2008) and Ducoin et al (2010).

At high angles of attack, airfoils/hydrofoils experience the well-known phenomenon of stall, which can occur in the form of a light stall with trailing edge separation, or a deep/massive stall in the form of leading edge separation (McCroskey 1982). In the case of a light stall, a quasi-steady vortex develops from the trailing edge and moves toward the leading edge, which decreases the lift and reduces the slope of the lift curve, $dC_L/d\alpha_{eff}$, as well as increases the drag (Rhie & Chow 1982). In the case of a massive stall, periodic shedding of the leading edge vortex is typically observed, which creates large load fluctuations and significant drops in lift such that the slope of the lift curve becomes negative, i.e., $dC_L/d\alpha_{eff} < 0$ (see, for example, Lee & Gerontakos (2004)), and significantly increases the drag.

The objective of this work is to investigate the effects of fluid structure interaction on the lift and drag coefficients of a hydrofoil in viscous flow, as well as changes in laminar to turbulent transition, static stall in lift, and divergence speed. In particular, the flow over a NACA66 hydrofoil is studied for initial angles of attack range from α_0=0° to 8° and freestream velocity range from V_∞=5 to 20 m/s. The fluid, solid, and FSI coupling models are presented, followed by a brief description of the experimental setup of the rigid and flexible hydrofoil studies. Comparisons of numerical predictions with experimental measurements are shown. The effects of FSI on viscous phenomena such as transition and stall are discussed, and the influence of viscous effects on the static divergence velocity is presented.

2 NUMERICAL MODEL

In this work, the hydrodynamic response of a flexible hydrofoil is simulated using the commercial CFD solver CFX; the plunging and pitching motion at the foil tip due to spanwise bending and twisting deformation of a 3-D, rectangular, cantilevered hydrofoil is simulated using a 2-DOF model. The fluid and solid solvers are coupled via a user-defined subroutine in CFX, which exchanges the fluid pressure field and foil motions between the solvers. A summary of the fluid model, solid model, numerical setup and boundary conditions, and FSI coupling algorithm is presented below.

2.1 Fluid Model

Fluid flow is described with the mass and momentum conservation equations, which are applied for an incompressible and viscous fluid:

$$\frac{\partial v_j}{\partial x_j} = 0 \tag{1}$$

$$\frac{\partial(\rho_F v_i)}{\partial t} + \frac{\partial(\rho_F v_i v_j)}{\partial x_j} = -\frac{\partial p}{\partial x_i} + \mu \frac{\partial^2 v_i}{\partial x_j \partial x_j} \tag{2}$$

where v_j, ρ_F, p, μ are the fluid velocity, density, pressure, and dynamic viscosity, respectively. The effects of gravitational force are assumed to be negligible.

The $k-\omega$ *SST* turbulence model was applied because it has been shown to be accurate for prediction of boundary layer detachments, see Menter (1993) and Haase et al (2006) for more details. The $k-\omega$ *SST* turbulence model is coupled with the $\gamma-Re_\theta$ transition model, which uses experimental correlations based on local variables (see Menter (2006) for details). The model is based on two transport equations. The first transport equation is for intermittency γ, which triggers the transition process. The second transport equation is for the transition momentum thickness Reynolds number, $Re_{\theta t}$. In this formulation, only local information is used to activate the production term in the intermittency equation. This model allows the capture of major transition effects and is accurate in the case of separation-induced transition. This model has already been validated with the NACA66 hydrofoil used in this paper and for the same operating conditions, as shown in Ducoin et al (2009a).

2.2 Solid Model

The plunging and pitching motion at the foil tip caused by spanwise bending and twisting of a 3-D, rectangular, cantilevered hydrofoil is represented using a 2-DOF model, as shown in Figure 1. The hydrofoil is assumed to be rigid in the chordwise direction; the spanwise bending, $h(z)$, and twisting, $\theta(z)$, deformations along the z-direction are assumed to be captured by the shape functions $f(z)$ and $g(z)$, respectively:

$$h(z) = h_0 f(z), \theta = \theta_0 g(z) \tag{2}$$

where h_0 is the vertical translation about the elastic axis, $\vec{X}_E = (x_E, y_E)$, at the foil tip defined positive downward, and θ_0 is the rotation about the elastic axis at the foil tip defined positive in the clockwise direction, as shown in Figure 1. It should be noted that $f(z)$ and $g(z)$ are obtained by applying the hydrodynamic pressure distributions (computed via CFX) on to a finite element model of the 3-

D, cantilevered, rectangular hydrofoil, and are found to be approximately the same for the range of angle of attacks of interest.

The hydrofoil is assumed to be located at an initial angle of attack α_0 from the uniform inflow in the x-direction. The resulting sectional lift (L_o) and drag (D_o) forces on the foil are applied at the center of pressure, $\vec{X}_P = (x_P, y_P)$, which is defined as follows:

$$\vec{X}_P = \frac{\int_0^C \vec{x} \times P(\vec{x}) d\vec{x}}{\int_0^C P(\vec{x}) d\vec{x}} \tag{3}$$

where c is the chord length, P is the local wall pressure, and $\vec{x} = (x, y)$ is the position vector.

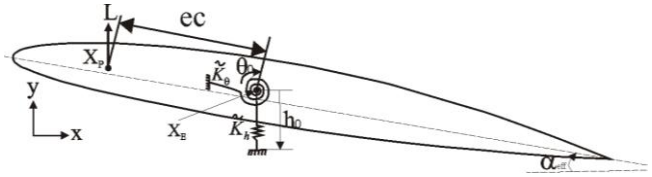

Figure 1: A 2-DOF model representing plunging (h_0) and pitching (θ_0) degrees of freedom at the tip of a 3-D, cantilevered, rectangular hydrofoil.

Static divergence is independent of time and hence inertial and damping forces are ignored in the equilibrium equation, which can be written as follows for a 2-DOF system (Bisplinghoff et al 1955):

$$\begin{bmatrix} \tilde{K}_h & \tilde{C}_{h\theta} \\ 0 & \tilde{K}_\theta - \tilde{C}_{\theta\theta} \end{bmatrix} \begin{bmatrix} h_0 \\ \theta_0 \end{bmatrix} = \begin{bmatrix} -\tilde{L}_0 \\ \tilde{T}_0 \end{bmatrix} \tag{4}$$

where $\tilde{K}_h$ and $\tilde{K}_\theta$ are respectively the generalized bending and torsional stiffness of the 3-D hydrofoil. It should be noted that "~" is used to denote the generalized terms, which accounts for the 3-D structural response by integrating the 2-D sectional terms (without the "~") along the spanwise direction using the appropriate shape functions.

The generalized lift force and moment terms, $\tilde{C}_{h\theta}$ and $\tilde{C}_{\theta\theta}$, associated with twist deformation are given by:

$$\tilde{C}_{h\theta} = qca \int_0^S g(z) f(z) dz \tag{6}$$

$$\tilde{C}_{\theta\theta} = qec^2 a \int_0^S g(z)^2 dz \tag{7}$$

where $q=0.5\rho_F V_\infty^2$ is the dynamic pressure, c is the chord length, $a=dC_L/d\alpha_{eff}$ is the slope of the lift curve, ec is the distance between the elastic axis and the center of pressure (as shown in Figure 1), s is the span length, and V_∞ is the inflow velocity.

The generalized lift and moment due to flow over a rigid hydrofoil are computed by integrating the section lift and moment (about the elastic axis) of the tip section (L_o and T_o) computed by the CFD solver along the spanwise direction using the corresponding shape functions $f(z)$ and $g(z)$:

$$\tilde{L}_0 = \int_0^S L_0 f(z) dz, \tilde{T}_0 = \int_0^S T_0 g(z) dz \tag{8}$$

The tip bending h_0 and the twist θ_0 motions can then be computed by solving Equation (4), which yields:

$$\theta_0 = \frac{\tilde{T}_0}{\tilde{K}_\theta - \tilde{C}_{\theta\theta}} \tag{9}$$

$$h_0 = \frac{-\tilde{L}_0 - \theta_0 \tilde{C}_{h\theta}}{\tilde{K}_h} \tag{10}$$

Static divergence occurs when the twisting capacity is reached, i.e.,

$$\tilde{K}_\theta - \tilde{C}_{\theta\theta} = 0 \tag{11}$$

The dynamic pressure and the speed at divergence can then be computed as follows:

$$q_{div} = \tilde{K}_\theta / (ec^2 a \int_0^S g(z)^2 dz) \tag{12}$$

$$V_D = \sqrt{\frac{2\tilde{K}_\theta}{\rho_F ec^2 a \int_0^S g(z)^2 dz}} \tag{13}$$

By applying Equations 12 and 13 into Equation 9, the following linear relationship between α_0/θ_0 and $1/V_\infty^2$ can be shown:

$$\frac{\alpha_0}{\theta_0} = V_D^2 \left(\frac{1}{V_\infty^2} - \frac{1}{V_D^2} \right) \tag{14}$$

where V_D is the square root of the slope of the α_0/θ_0 versus $1/V_\infty^2$ curve.

2.3 Numerical Setup and Boundary Conditions

To demonstrate and validate the numerical model, results are shown for a cantilevered rectangular hydrofoil. All the results shown in this paper correspond to a Naca66 hydrofoil held fixed in place at its root inside a water tunnel at the French Naval Academy (IRENav), France. Readers should refer to Leroux et al (2005) for more details about the experimental setup. The nominal free stream velocities range from V_∞=5 m/s to 20m/s, which yields a moderate to high Reynolds number of $Re=V_\infty c/\nu=0.75\times10^6$ to 3×10^6. The density and dynamic viscosity of the liquid are taken to be ρ_F=999.19 kg/m^3 and $\mu=\nu\rho_F$=1.139 Pa·s, respectively, which correspond to fresh water at 15°C. The 2-D fluid domains considered are shown in Figure 2.

Two fluid meshes are used in this paper:

- Mesh 1 has boundaries that match the experimental test section of the hydrofoil measurements carried out at the French Naval Academy. This case has a significant confinement effect due to top and bottom wall boundaries, particularly when the foil is placed at high angles of attack.
- Mesh 2 has infinite boundaries, and is used for the static divergence studies to avoid

confinement effect caused by high angles of attack and large elastic foil deformations.

For both meshes, the distances between the elastic axis and the upstream and downstream boundaries are 5.474c and 9.526c, respectively. A no-slip boundary condition is imposed on the hydrofoil surface, and symmetry conditions are imposed on the top and bottom boundaries of the tunnel. The inlet velocity and the outlet reference pressure are set. A constant turbulent intensity of 2% is set at the inlet boundary and is equal to the experimentally measured turbulent intensity.

All the coupled FSI runs are initialized with steady-state calculations. The 2-D fluid mesh shown in Figure 2 (a) corresponds to the confined case, and is composed of 120,000 elements with 50 structured elements across the boundary layer, which is selected to ensure $y_+ \approx 1$. The regions outside the boundary layer are discretized with unstructured triangular elements. Mesh refinements are performed at the foil leading edge, trailing edge, and in the wake region. The 2-D fluid mesh shown in Figure 2 (b) corresponds to the infinite boundary case, and has approximately the same number of elements since a coarser mesh is used in the region far away from the hydrofoil, while similar mesh characteristics and densities as the confined case are used near the hydrofoil.

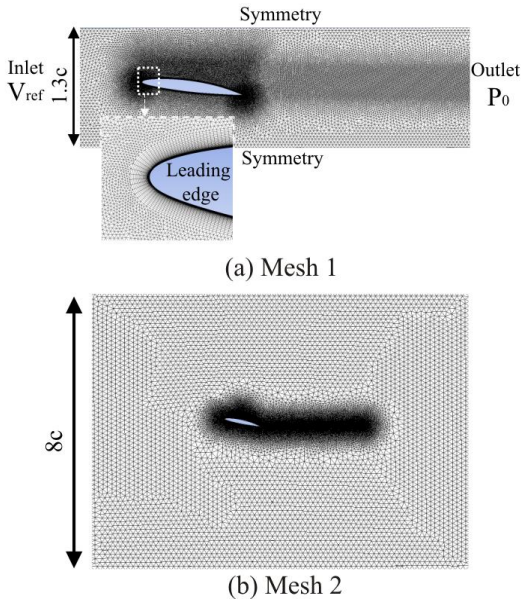

Figure 2: (a) Mesh 1 corresponds to the experimental facility with the tunnel walls; (b) Mesh 2 corresponds to the infinite boundary case, for use in the static divergence study.

Second order schemes are used in all the fluid computations. The time integrator scheme is a second-order backward Euler scheme, and the spatial derivatives are computed using a second-order upwind scheme. Mesh convergence and time discretization were studied in detail for the case of a fixed, rigid hydrofoil at an angle of attack of α_0 = 6° in steady flow; see Ducoin et al (2009a) for more details.

2.4 FSI coupling algorithm

The foil displacement is applied after the fluid solution convergences for the fixed, rigid body problem. A user-defined function in CFX is used to update the foil boundary according to the plunging and pitching motions computed via Equation 4, and the entire fluid mesh is updated to accommodate the foil deformations. An explicit, loose-coupling method is used because only steady-state results are shown in this work.

To enhance convergence, the displacements are under-relaxed during the first 0.1 s of the coupled FSI calculation. The structure time step size, Δt_s=0.01 s, is set to be 10 times the fluid time step size, Δt_f=0.001 s, to reduce remeshing/computational cost since it is not necessary to use such a fine time step size to capture the foil motion in the 2-DOF model. The convergence criterion requires the change in the average values of h_0, θ_0, C_L, and C_D over 10 structure time steps normalized by the average values of the 10 previous time steps to be less than $1e^{-4}$. C_L, and C_D are respectively the 2D sectional lift and drag coefficients, defined as:

$$C_L = \frac{L_0}{0.5\rho V_\infty{}^2 c} \tag{15}$$

$$C_D = \frac{D_0}{0.5\rho V_\infty{}^2 c} \tag{16}$$

3 EXPERIMENTAL MODEL

Results from two sets of experiments in water tunnel involving a rigid hydrofoil and a flexible hydrofoil are used to validate the numerical simulations. The rigid hydrofoil was made of stainless steel (Young's modulus E=210,000 MPa, solid density ρs=7,800 kg/m3, and poisson's ratio νs=0.3) and the flexible hydrofoil was made of POM Polyacetate (E=3,000 MPa, ρs=1,480 kg/m3, and νs= 0.35). Both sets of experiments were conducted in the same water tunnel facility, and the initial un-deformed geometries of both hydrofoils were made to be identical. The test section is 1 m long and has a 0.192 m square section. The velocity can range between 0 and 15 m/s and the pressure from 30 mbar to 3 bars. The cross-section of the foil has a NACA 66 thickness distribution with a maximum thickness-to-chord ratio of 12%, and a NACA a=0.8 camber distribution with a maximum camber-to-chord ratio of 2%. The chord length is c=0.15 m and the span length is s=0.191 m. The objective of the experimental study is to investigate FSI effects by comparing the performance of the rigid and flexible hydrofoils.

The lift and drag forces acting on the rigid hydrofoil were measured using a resistive gauge hydrodynamic balance with a range up to 150 daN in lift and 15 daN in drag. Readers should refer to Leroux et al (2005) for additional details about the rigid hydrofoil experimental setup and results. The tip section displacement of the flexible hydrofoil was measured using a high-speed video camera

PHOTRON. Readers should refer to Ducoin et al (2009b) for more details about the flexible hydrofoil experimental setup and results.

4 RESULTS

4.1 Validation with experiments

To validate the solvers, numerical predictions are compared with experimental measurements of the rigid and flexible hydrofoil described above. Figure 3 (a) shows the comparison of lift coefficients (C_L) for the rigid hydrofoil, and Figure 3 (b) shows the comparison of tip section displacements (δ_y) measured at the leading edge for the flexible hydrofoil. In Figure 3, the numerical predictions using the confined fluid domain (Mesh 1 in Figure 2) and infinite fluid domain (Mesh 2 in Figure 2) are shown together with the measured values to illustrate the effects of the tunnel walls. Good general agreements are observed for the lift coefficient. The change in slope of the lift curve around $\alpha_0 \approx 5°$ is due to laminar to turbulent transition. Indeed, it has been shown in Ducoin et al (2009a) that under $\alpha_0 \approx 5°$, the boundary layer is mostly laminar due to the laminar cross-section (NACA66) of the hydrofoil, even though the Reynolds number is relatively high. The laminar to turbulent transition is located near the trailing edge and is triggered by a Laminar Separation Bubble (LSB). Around $\alpha_0 \approx 5°$, the high pressure gradient at the leading edge induced by the leading edge curvature induces a second laminar separation at the leading edge and the flow transitions suddenly to turbulent. The transition has a strong effect on hydrodynamic characteristics. The results suggest that the structure (tip section displacement) responds linearly to the hydrodynamic loading, confirming hydroelastic response. The effects of transition can also be observed in the change in slope of the displacement curve.

As expected, the numerical results obtained using the confined mesh matched better with the experimental measurements, as it was conducted inside a confined water tunnel. For the range of angles of attacks considered, the hydrofoil blockage effect in the *y*-direction increased the fluid velocity by about 10-15%, which increased the lift coefficients and tip section displacements. However, the slopes of the lift coefficient and displacement curves for both the confined and infinite boundary cases are quite similar.

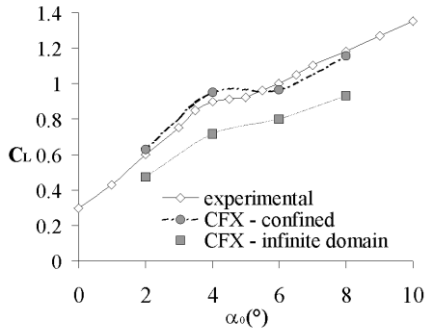

(a) Rigid hydrofoil

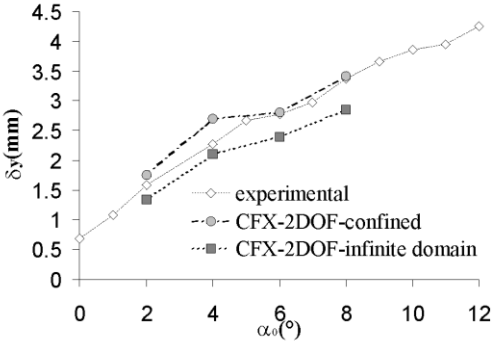

(b) Flexible hydrofoil

Figure 3: Comparisons of the measured vs. predicted lift coefficient for the rigid hydrofoil (a), and tip section displacements for the flexible hydrofoil (b). Both cases involve fully wetted flows with Re=750,000 and V_∞ =5m/s.

4.2 Influence on viscous effects on the FSI response

The aim of this section is to investigate the viscous FSI response of the flexible hydrofoil, including laminar to turbulent transition, stall, hydrofoil performances and deformations. To avoid confinement effects, the numerical predictions are obtained using infinite domain mesh.

To investigate boundary layer flow modifications due to structure deformations, Figure 4 shows the predicted effective angle of attack, $\alpha_{eff}=\alpha_0+\theta_0$, as a function of the free-stream velocity, V_∞, for cases with different initial angles of attack, α_0. For low velocities, the deformations are negligible due to the weak loading, and hence $\alpha_{eff} \approx \alpha_0$. As the loading increases with the square of V_∞, the effective angle of attack increases. The trend changes around $\alpha_{eff} \approx 13°$ because of static stall, which is associated with decreases in lift and deformation, and increases in drag. The maximum value for α_{eff} is limited to approximately 13°- 14° because of static stall, which in turn affects the static divergence, as will be shown later in this paper.

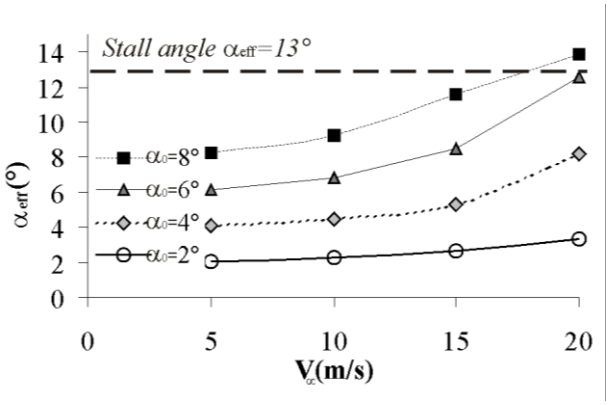

Figure 4: Effective angle of attack of the flexible hydrofoil versus free-stream velocity for different initial angles of attack α_0. Fully wetted flow conditions.

To understand the evolution of twist deformation and static divergence, it is necessary to analyze the evolution of the center of pressure, which determines the hydrodynamic moment along with the lift, as α_0 and V_∞ increase. As shown in Figure 5, the center of pressure moves toward the leading edge as the angle of attack increases. For the rigid hydrofoil, small variations are observed between the different free-stream velocities considered, and are due to Reynolds number effects. For the flexible hydrofoil operating in low velocities, V_∞ =5m/s, the center of pressure moves linearly with α_0 toward the leading edge (located at X/c=0), with almost negligible difference from the rigid hydrofoil case. For V_∞ =5m/s and α_0 = 8°, the center of pressure is located at X/c=0.29 for the rigid hydrofoil, and is located at X/c=0.28 the flexible hydrofoil. For the flexible hydrofoil operating at higher V_∞, the twist angle increases due to the higher loading, and the center of pressure moves closer to the leading edge. Therefore, its distance from the elastic axis, *ec*, increases, which will increase the hydrodynamic moment about the elastic axis. When stall and leading edge vortex shedding occurs (α_0=6° and 8°, V_∞=20 m/s, *Re*=3,000,000), the pressure distribution is modified, and the center of pressure fluctuates (as indicated by the large error bar in Figure 5) and moves closer to the midchord location, which will conversely decrease the hydrodynamic moment about the elastic axis.

Figure 6 shows the evolution of transition point along the chord for the rigid and flexible hydrofoils. In this work, the transition point is defined as the point of turbulent re-attachment, where the skin friction coefficient is equal to zero. It is observed that the transition point moves toward the leading edge as the angle of attack increases until it becomes approximately flat at α_0=6°.

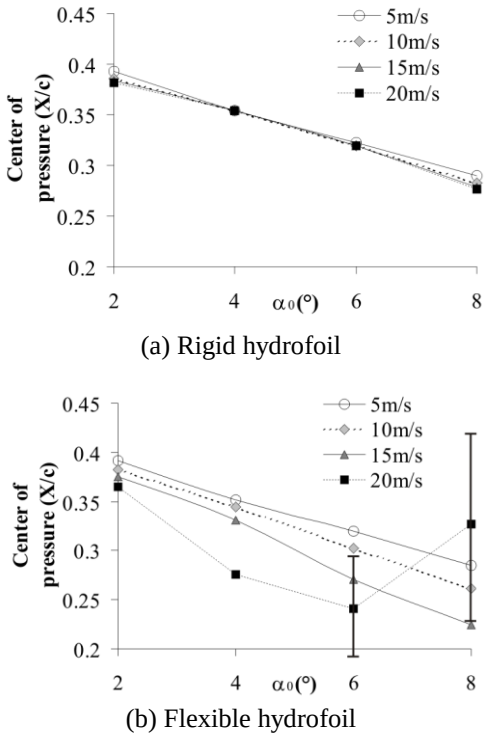

(a) Rigid hydrofoil

(b) Flexible hydrofoil

Figure 5: Evolution of the center of pressure for (a) the rigid hydrofoil and (b) the flexible hydrofoil. The foil leading edge is at X/c=0, and the foil trailing edge is at X/c=1.

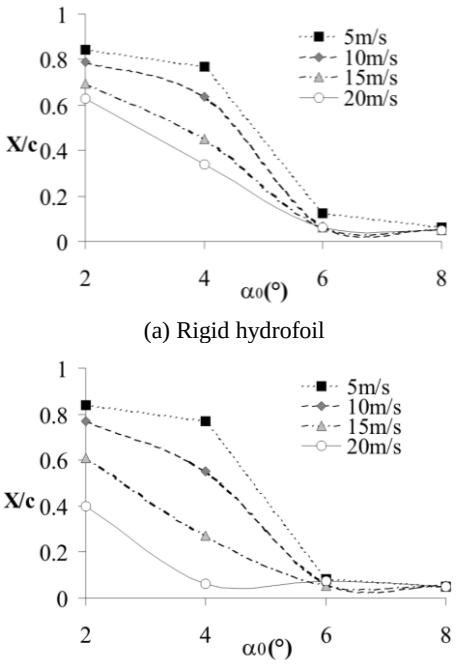

(a) Rigid hydrofoil

(b) Flexible hydrofoil

Figure 6: Evolution of the transition point for (a) the rigid hydrofoil and (b) the flexible hydrofoil.

As the flow velocity or Reynolds number increases, the transition point moves progressively toward the leading edge for the same α_0, which smoothes the transition to turbulence. The comparisons between rigid and flexible hydrofoils show that the deformations promote transition

to turbulence because of the higher effective angle of attack caused by the clockwise twisting of the flexible hydrofoil about the elastic axis. A greater difference is observed for the highest loading with V_∞=20 m/s, where the transition point moves to be near the leading edge at α_0=5°. Separation and vortex shedding are generated at the leading edge. It is observed that with the twist deformation θ_0, the effective angle of attack can reach the stall point around 13°, as shown in Figure 4.

Figure 7 compares the axial flow velocity contour for the rigid and flexible hydrofoils at V_∞=20 m/s. It is observed that twist deformation is high enough to induce massive stall for α_0=6° and 8°, where the effective angles of attack reached respectively α_{eff}=13° and α_{eff}=14°.

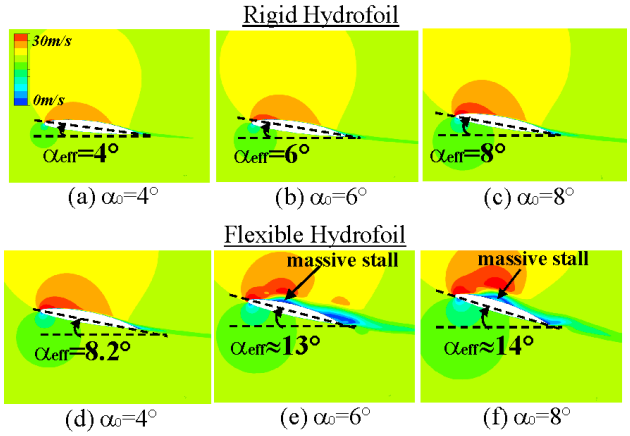

Figure 7: Velocity contours for the rigid and flexible hydrofoils, Re=3,000,000, V_∞=20m/s.

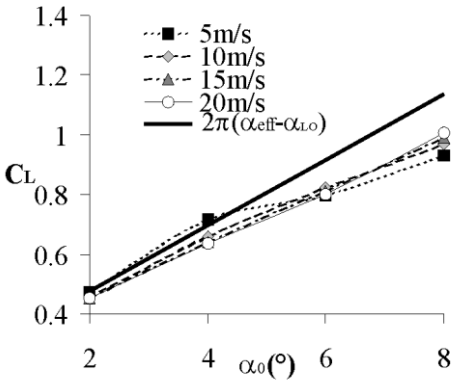

(a) Rigid hydrofoil

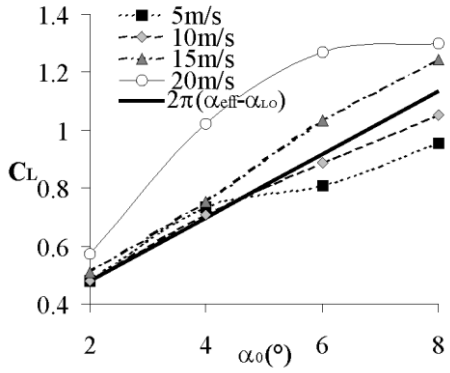

(b) Flexible hydrofoil

Figure 8: Predicted lift coefficients for (a) the rigid hydrofoil and (b) the flexible hydrofoil as a function of initial angle of attack α_0.

The lift (C_L) and drag (C_D) coefficients are show in Figure 8 and 9, respectively, as functions of the initial angle of attack. In Figure 8, the line representing the ideal lift coefficient, $2\pi(\alpha_{eff}-\alpha_{OL})$ with α_{OL} as the zero lift angle of attack), for a rigid lifting surface is also shown for comparison. In general, the lift coefficient of the flexible hydrofoil is higher than the rigid hydrofoil due to the higher effective angle of attack caused by the clockwise twist motion induced by the fluid loading with the center of pressure to the left of the elastic axis. The elastic twist motion tends to increase the drag coefficient for V_∞ > 10 m/s.

At V_∞=5 m/s, the transition to turbulence at the leading edge induces a decrease in performance between α_0=4° and 6°, where the lift coefficient decreases and the drag coefficient increases. As V_∞ increases, differences in result due to Reynolds number effects become negligible. At highly loaded conditions, V_∞=15 and 20 m/s, the twist deformation becomes high enough to reach the stall point, where the flow becomes fully detached at α_{eff}≈13°, as shown in Figure 7 (e) and (f). As a consequence, the lift coefficient decreases and the drag coefficient increases nonlinearly because of flow separation and the presence of vortex shedding at the hydrofoil surface.

The analysis of viscous effects on hydrodynamic coefficients shows that viscosity can change the slope of the lift curve, $dC_L/d\alpha_{eff}$, and the position of the center of pressure enough to strongly modify the divergence speed, compared to inviscid computation:

- In the case of the laminar to turbulent transition around α_{eff}=5°, viscous effect lead to decreases in $a=dC_L/d\alpha_{eff}$, which will increases the divergence speed V_D (according to Equation 13) compared to inviscid flow.
- When the angle of attack becomes too high, the slope of the lift curve decreases due to stall and the movement of the center of pressure toward the midchord point, both of which tend to delay static divergence.

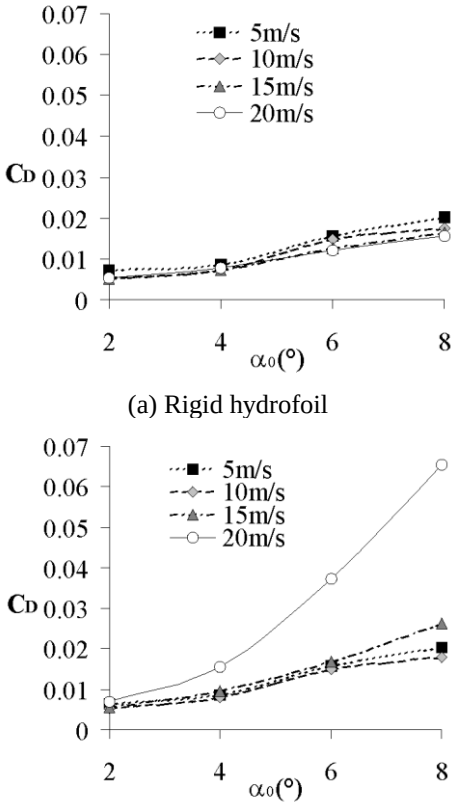

(a) Rigid hydrofoil

(b) Flexible hydrofoil

Figure 9: Drag coefficients for (a) the rigid hydrofoil and (b) the flexible hydrofoil as a function of initial angle of attack α_0.

4.3 Static Divergence

The aim of this section is to calculate the static divergence velocity, and highlight the possible nonlinear viscous effects. Figure 10 shows the evolution of α_0/θ_0 versus $1/V_\infty^2$ for the flexible hydrofoil with different values of α_0. According to Equation 14, α_0/θ_0 should be a linear function of $1/V_\infty^2$ with the slope of the curve equal to V_D^2, the y-intercept to be -1 and the x-intercept to be at $1/V_\infty^2=1/V_D^2$. A linear relationship is observed in Figure 10. According to linear, potential flow theory, the slope of the curve shown in Figure 10 (and hence the divergence speed) does not vary with different α_0 for a given hydrofoil because the slope of the lift curve, $a=dC_L/d\alpha_{eff}$, is constant, and the distance between the elastic axis and the center of pressure is assumed to be constant at $ec=c/4$. However, small deviations in the slope are observed in Figure 10 for different values of α_0 because (1) changes in the slope of the lift curve, a, as shown in Figure 8, and (2) changes in the center of pressure (i.e., ec) as shown in Figure 5. These changes from potential flow assumptions are due to viscous effects, which govern laminar to turbulent transition at low speeds, and flow separation at high speeds and high angles of attack.

The Young's modulus of the flexible hydrofoil made of POM Polyacetate is E=3000 MPa, which gives a calculated divergence velocity at V_∞=5m/s of V_D=28.8 m/s according to potential theory, and V_D=31.8-29.6m/s for α_0=2°-8° according to viscous flow computations.

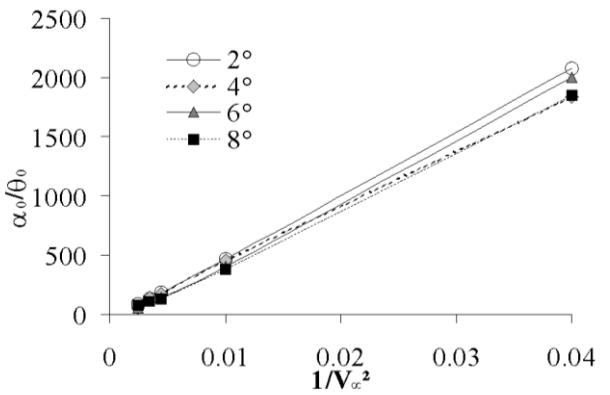

Figure 10: Evolution of twist deformation as a function of $1/V_\infty^2$ for various upstream velocities.

The results clearly illustrate the importance of fluid viscous effects in the FSI response and in the calculation of the static divergence velocity. Nevertheless, substitution of values for a and ec based on potential theory into Equation 13 are still useful to obtain a first order estimation of V_D, and to determine how V_D changes with torsional stiffness and fluid density.

5 CONCLUSION

In this paper, the hydroelastic response and stability of a flexible hydrofoil in viscous flow are investigated using a 2D RANS solver (CFX) coupled with a 2-DOF solver representing the tip bending and twisting motions of a cantilevered hydrofoil. The operating conditions (Re=0.75 × 10^6 to 3 × 10^6, α_0=2° to 8°) were chosen to obtain loading conditions representing different flow regimes. The FSI solver was validated by comparing numerical predictions with experimental measurements of a rigid and a flexible hydrofoil conducted at the French Naval Academy, France. The results show that the flexible hydrofoil undergoes a clockwise rotation about the elastic axis because the center of pressure is to the left of the elastic axis, which in turn increases the effective angle of attack. The increase in effective angle of attack caused by the elastic deformation accelerates transition and stall, and changes the location of the center of pressure, all of which result in nonlinearities that have strong effects on the FSI response and static divergence. At low speeds, laminar to turbulent transition reduces the slope of the lift curve, which helps to delay stall. At highly loaded conditions where the flow is fully turbulent, the effective angle of attack, and hence the lift coefficient, of the elastic hydrofoil increases nonlinearly with α_0 and V_∞ because the center of pressure shifts toward the leading edge; this nonlinear increase decays as the foil moves toward stall, at which point the slope of the life curve becomes negative and the center of pressure fluctuates while moving toward the midchord point; hence, viscous effects associated with stall also helps to delay divergence.

This work presents a method to compute the static divergence speed of a flexible hydrofoil with consideration for viscous effects. The proposed method

can be extended for the analysis of general 3-D blade sections by employing appropriate shape functions representing the deformation along the spanwise direction, as well as the effective 3-D generalized bending and twisting stiffness values, to provide a first-order estimate of the coupled response and divergence speed. As shown in Liu and Young (2010), the general form of Equation (14) still holds for a 3-D composite marine propeller, and can be used to estimate the static divergence speed of general 3-D structures. Nevertheless, since 3-D effects are known to be important for marine propellers, particularly at the blade tip, a fully coupled 3-D FSI model is recommended. Additional studies are also needed to investigate dynamic FSI effects in viscous flow, including changes in vibration characteristics due to transition, load fluctuations associated with large scale shedding of vortices (as observed in Ducoin et al 2009a), as well as potential resonance and flutter issues.

ACKNOWLEDGMENT

The authors gratefully knowledge the Office of Naval Research (*ONR*) and Dr. Ki-Han Kim (program manager) for their financial support through grant number N0014-09-1-1204.

REFERENCES

Bisplinghoff, R., Ashley, H. & Halfman, R. (1996). Aeroelasticity. Dover Publications.

Chang, P. A., Elbert, M., Young, Y. L, Liu, Z., Mahesh, K., Jang, H. & Shearer, M. (2008). 'Propeller Forces and Structural Response due to Crashback'. 27th Symposium on Naval Hydrodynamics, Seoul, Korea.

Ducoin, A., Astolfi, J. A., Deniset, F. & Sigrist, J. F. (2009a). 'Computational and experimental investigation of flow over a transient pitching hydrofoil'. European Journal of Mechanics/B Fluids **28**, pp. 728–743.

Ducoin, A., Astolfi, J. A., Deniset, F. & Sigrist, J. F. (2009b). 'An experimental and numerical study of the hydroelastic behavior of an hydrofoil in transient pitching motion'. First International Symposium on Marine Propulsion SMP09, Trondheim, Norway.

Ducoin, A., Astolfi, J. A. & Gobert, M. L., (2010). 'An experimental study of boundary-layer transition induced vibrations on a hydrofoil'. FEDSM2010, Montreal, Canada.

Edwards, J. & Wieseman, C. (2008). 'Flutter and divergence analysis using the generalized aeroelastic analysis method'. Journal of Aircraft **45**(3), pp. 906–915.

Fung, Y. (2002). An introduction to the theory of aeroelasticity. Dover Publications.

Gaster, M. (1969). The Structure and Behaviour of Laminar Separation Bubbles. HMS O.

Haase, W., Aupoix, B., Bunge, U. & Schwamborn, D. (2006). FLOMANIA-A European Initiative on Flow Physics.

Lee, T. & Gerontakos, P. (2004). 'Investigation of flow over an oscillating airfoil'. Journal of Fluid Mechanics **512**, pp. 313–341.

Leroux, J. B., Coutier-Delgosha, O. & Astolfi, J. A. (2005). 'A joint experimental and numerical study of mechanisms associated to instability of partial cavitation on two-dimensional hydrofoil'. Physics of Fluids **17**, 052101.

Librescu, L. & Thangjitham, S. (1991). 'Analytical studies on static aeroelastic behavior of forward-swept composite wing structures'. Journal of aircraft **28**(2), pp. 151–157.

Librescu, L. & Maalawi, K. (2009). 'Aeroelastic design optimization of thin-walled subsonic wings against divergence'. Thin-Walled Structures **47**(1), pp. 89–97.

Liu, Z. & Young, Y. L. (2010). 'Static divergence of self-twisting marine propellers'. Journal of Fluids and Structures **26**, pp. 841-847.

Poirel, D., Harris, Y. & Benaissa, A. (2008). 'Self-sustained aeroelastic oscillations of a NACA0012 airfoil at low-to-moderate Reynolds numbers'. Journal of Fluids and Structures **24**(5), pp. 700–719.

McCroskey, W. (1982). 'Unsteady airfoils'. Annual Review of Fluid Mechanics **14**(1), pp. 285–311.

Menter, F. R. (1993). 'Improved Two-Equation k-Turbulence Models for Aerodynamic Flows'. NASA Technical Memorandum **103975 34. 38**.

Menter, F. R., Langtry, R. & Volker, S. (2006). 'Transition Modelling for General Purpose CFD Codes, Flow'. Turbulence and Combustion **77**(1), pp. 277–303.

Rhie, C. & Chow, W. (1983). 'Numerical study of the turbulent flow past an airfoil with trailing edge separation'. AIAA Journal **21**, pp. 1525–1532.

Thomas, J., Dowell, E. & Hall, K. (2002). 'Nonlinear inviscid aerodynamic effects on transonic divergence, flutter, and limit-cycle oscillations'. AIAA journal **40**(4), pp. 638–646.